Experimental characterization of the dynamic failure behavior of mortar under impact loading

D. L. Grote, S. W. Park,[a)] and M. Zhou[b)]

The George W. Woodruff School of Mechanical Engineering, Georgia Institute of Technology, Atlanta, Georgia 30332-0405

The failure behavior of mortar under dynamic impact loading is characterized through a series of plate impact experiments. The analysis focuses on the spall strength and the shear stress carrying capacity in different regions of the specimen under normal impact loading. Special attention is paid to the possible existence of a failure wave phenomenon that has been widely recognized as an important failure mechanism for glasses during plate impact. The experiments are designed to allow the strengths of the medium at locations behind and ahead of a possible failure wave front to be analyzed. The diagnostics used include velocity interferometer system for any reflector (VISAR) recording of the free surface velocities of targets and monitoring of the internal stresses via polyvinylidene fluoride (PVDF) gauges embedded in the specimen. Experiments conducted do not provide evidence for the existence of a failure wave phenomenon for mortar under plate normal impact loading. While the study suggests that a threshold impact stress must be exceeded for failure to occur, a clearly defined failure wave that propagates behind the loading wave is not observed. Instead, a gradual failure process that initiates upon the arrival of the loading wave and progresses thereafter is observed. This gradual failure process in mortar is in contrast to the well-defined failure front and complete loss of tensile strength associated with the failure wave phenomenon reported for glasses. The study also indicates that, under impact involving high levels of input stresses, attenuation of the loading wave occurs as it propagates through the failed medium. © *2001 American Institute of Physics.* [DOI: 10.1063/1.1340005]

I. INTRODUCTION

The ''failure wave'' phenomenon has been reported and analyzed extensively for glasses.[1–9] This phenomenon occurs during normal impact of planar specimens. Once a threshold impact stress is exceeded, a well-defined failure wave propagates behind the compressive loading wave from the impact face toward the interior of the stressed specimen. The reported threshold impact stress is near but below the Hugoniot elastic limit (HEL) and the failure wave propagates at a speed lower than the longitudinal wave speed of the material. The failure wave front separates the intact material ahead of the failure wave and the comminuted material behind it. The process involves a total loss of spall strength and a significant drop in shear strength of material traversed by the failure wave.

Brar *et al.*[1] and Kanel *et al.*[2] reported the failure wave phenomenon in a series of impact experiments with glass plates and bars. Investigations by Brar *et al.*[1] and Brar and Bless[10] suggested that a threshold impact stress must be exceeded for a failure wave to occur. Before the existence of the failure wave was confirmed, Rosenberg *et al.*[11] noticed a sharp drop in spall strength relative to the HEL after the failure wave passes the point of observation. Raiser,[12] through his experiments on aluminosilicate glass, found that the spall strength drops, the transverse stress increases, the shear strength decreases, and the medium experiences a general breakup within the region traversed by the failure wave. Recently, analytical modeling and numerical simulation of the failure wave phenomenon has received growing attention.[7–8]

Raiser[12] and Clifton[3] suggested that a phase transformation to a crystalline structure is the most likely cause of the failure wave phenomenon. However, other researchers have since obtained results that contradict this argument. For instance, Espinosa *et al.*[6] presented two possible causes that may be responsible for the phenomenon. The first is the initiation of microcracks at the surface subjected to compressive traction and their propagation into the interior of the material along planes of maximum shear stress. The second involves shear-induced plastic flow surfaces punched into the bulk of the material. Their analysis of postimpact samples yielded no evidence supporting a phase change in the material. There is currently no consensus on the actual cause of failure behind the failure wave. Espinosa *et al.*[6] noted, however, that microcracking is mainly responsible for the progressive decay behind the failure wave front. There is a consensus that microcracking plays an important role in this process.

Although the failure wave phenomenon has widely been recognized for glasses, the same has not been reported to date for geologic materials under shock or impact loading.[13–16] Chen and Xin,[8] based on the concept of local dilatation, suggested that a similar phenomenon may exist in

---
a)Current address: U.S. Federal Highway Administration, TFHRC, McLean, Virginia 22101.
b)Author to whom all correspondence should be addressed, 404-894-3294; Electronic mail: min.zhou@me.gatech.edu

TABLE I. Composition of the fly ash used in mortar specimens.

Components	Volume (%)	ASTM C618 Spec. (Class F)	AASHTO M295 Spec. (Class F)
Silicon dioxide (SiO_2)	50.7	⋯	⋯
Aluminum oxide (Al_2O_3)	24.9	⋯	⋯
Iron oxide (Fe_2O_3)	13.8	⋯	⋯
Sum of SiO_2, Al_2O_3, and Fe_2O_3	89.4	70.0% Min.	70.0% Min.
Calcium oxide (CaO)	3.1	⋯	30.0% Max.
Magnesium oxide (MgO)	1	⋯	5.0% Max.
Sulfur trioxide (SO_3)	0.5	5.0% Max.	5.0% Max.
Moisture content	0.2	3.0% Max.	3.0% Max.
Loss on ignition	3.6	6.0% Max.	5.0% Max.
Amount retained on No. 325 sieve	22	34.0% Max.	34.0% Max.
Specific gravity	2.31	⋯	⋯

geologic materials because their mechanical properties are pressure dependent. Indeed, the significant proportion of sand (or glass) in the compositions of concrete and mortar suggests there is a possibility that a failure mechanism similar to the failure wave phenomenon may exist in these materials.

The current study focuses on the failure behavior of mortar under the uniaxial strain conditions of normal plate impact. Mortar is selected over concrete mainly because of its enhanced homogeneity in microstructure compared with concrete. The experiments are designed to allow the tensile and shear strengths of the specimen material at locations behind and ahead of a possible failure wave to be analyzed. The diagnostics used include velocity interferometer system for any recorder (VISAR) recording of the free surface velocities of targets and monitoring of internal stresses via polyvinylidene fluoride (PVDF) gauges embedded in the specimens. Experiments conducted are expected to reveal the characteristics of the failure process under the conditions of uniaxial strain induced by normal plate impact.

II. MATERIALS

The material analyzed is a G-mix mortar provided by Wright Laboratory at Tyndall Air Force Base. The mortar has a nominal density of 2100 kgm^{-3} and a longitudinal wave speed of 4031 ms^{-1}. All samples were water cured for 28 days. Fly ash is used to facilitate the mixing of wet mortar, allowing a decrease in the level of moisture. This process allows the mix to possess the ideal moisture level for highest strength. The composition of the fly ash used in mortar specimens is given in Table I. Figure 1 shows a representative cross section of a mortar specimen. An inspection of the specimen revealed the presence of voids on its surfaces with a maximum size on the order of 0.5 mm. Table II lists the material constants for mortar and polymethylmethacrylate (PMMA) used in the experiment.

III. EXPERIMENTS

A schematic illustration of the impact configuration is shown in Fig. 2. The impact involves a PMMA flyer and a mortar target, with projectile velocities between 54 and 482 ms^{-1}. The thicknesses of the flyer and target and the impact

velocity for the experiments conducted are summarized in Table III. A gap between the flyer and the projectile tube is provided to ensure a traction-free end condition at the back surface of the flyer during the impact process. All plate impact experiments were carried out in the High Strain Rate Laboratory at Georgia Institute of Technology.

Two different types of diagnostics are employed. The first one uses a VISAR to monitor particle velocity histories at the rear surface of impacted specimens. The VISAR unit has an accuracy of ± 2 ms^{-1}. The second type of diagnostics uses PVDF stress gauges to measure the histories of longitudinal and transverse stresses in the interior of the specimens. The stress gauges have an accuracy of 0.2% for longitudinal stress measurement. So far, no application of such gauges for transverse stress measurement has been reported. An elastic impact experiment was conducted in this study to calibrate the gauges for such transverse stress measurement. It is found that the error associated with transverse measurement is approximately 11% for the peak stress. This is considered quite good since the error for transverse measure-
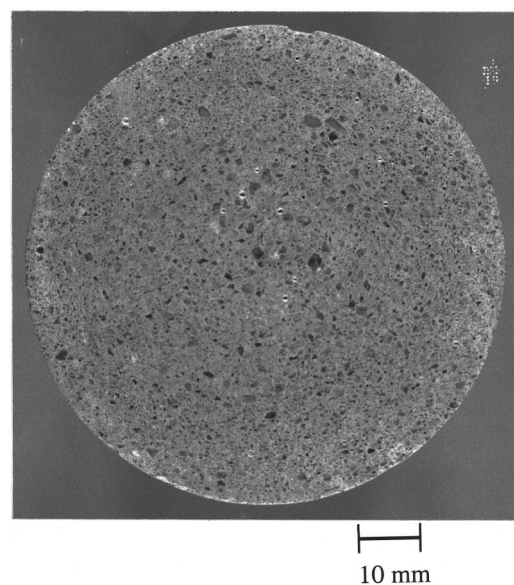

FIG. 1. Cross section of a mortar specimen before experiment (diameter: 76.2 mm).

TABLE II. Material constants.

Material	Density (kg-m^{-3})	Young's Modulus (GPa)	Poisson's Ratio	Longitudinal wave speed (ms^{-1})	Rayleigh wave speed (ms^{-1})
Mortar	2100	30.7	0.20	4031	2242
PMMA	1190	3.10	0.35	2045	918

ment comes from two sources. The first is due to the compressive strain in the impact direction and the second is due to the time it takes for stress waves to traverse the finite width of the active gauge area in the direction of impact. More details for this calibration are provided in the Appendix.

This analysis is carried out in a way that the failure behavior of the material at hand is compared with the characteristics of the failure wave phenomenon in glasses. To this end, the experiments focus on the tensile and shear strengths at different locations within the specimen during impact loading. Three sets of experiments are conducted in order to confirm or rule out the existence of a failure wave phenomenon in the mortar analyzed.

The first set of experiments focuses on the spall strength of mortar as the postulated failure wave propagates through the specimen. Time–distance diagrams for the experiments conducted are shown in Figs. 3(a) and 3(b). Longitudinal wave fronts are represented by solid lines while the postulated failure wave fronts are represented by dashed lines. These fronts are predicted using the Rayleigh wave speed (c_R) listed in Table II. The failure wave speed is assumed to be $c_f = c_R / \sqrt{2}$. This assumption is proposed by Raiser[12] based on the experimental observation of Brar et $al.$[1] Specifically, it assumes that cracks associated with a failure wave front propagate at the limiting speed of c_R in directions $\pm 45°$ relative to the direction of wave propagation. The location of the spall plane, denoted by point A, differs in the two configurations illustrated schematically in Figs. 3(a) and 3(b). In Fig. 3(a), tensile loading occurs behind the failure wave front, allowing the tensile (or spall) strength of the damaged material to be probed. In Fig. 3(b), tensile loading occurs ahead of the failure wave front, allowing the spall strength of the undamaged material to be analyzed.

If the loading is of sufficiently large amplitude to initiate failure and if a failure wave indeed exists, the failed material would have essentially zero spall strength, allowing the material to open up (or spall) under the tensile stresses. This spall process provides a free surface, allowing the tensile wave to be reflected as a compressive wave and propagate toward the back surface of the target. Consequently, an increase in surface velocity will be observed at point B in Fig. 3(a). If there is no failure wave, the material at A would retain its original strength and no pull-back (or recompression) signal would be registered at B. Figure 3(b) represents the case in which the spall plane lies ahead of the failure wave. The spall strength, in this case, would not be affected by the presence of a failure wave. It is to be noted that the cylindrical release waves disrupt the one-dimensional nature of loading in the specimen and limit the time window of valid data acquisition. In these two configurations, the cylindrical release waves arrive at the location of velocity measurement at the center of specimen surface approximately 9.73 and 10.45 μs after impact, respectively.

The second set of experiments focuses on the analysis of the shear strength of impacted specimens. PVDF stress gauges are imbedded in the specimens to measure the longitudinal and transverse stress histories during impact, [see Fig. 4(a)]. The PVDF gauges allow the direct measurement of stresses inside the specimen or on the impact face. These gauges make use of the piezoelectric effect of ferroelectric polymeric thin films.[17–19] The experiments use the fact that the material loses part of its shear strength upon failure. This reduction in shear strength is reflected as a reduction in the difference between the longitudinal and transverse stresses. A sharp rise in the transverse stress during impact would indicate that the material at the gauge location has undergone failure under compression. The center of the transverse gauge is positioned approximately 6 mm from the impact face, and the longitudinal gauge is placed 1.5 mm behind the transverse gauge (farther away from the impact face).
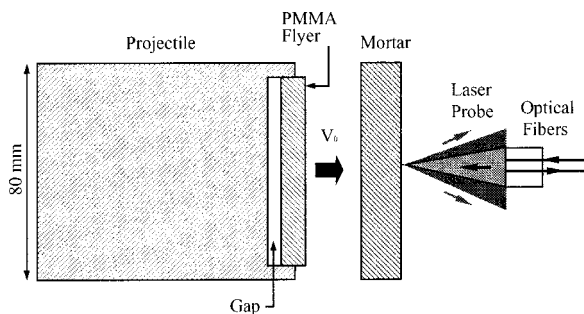

FIG. 2. Schematic configuration of plate impact experiment.

TABLE III. Summary of impact conditions.

Shot ID	PMMA flyer thickness (mm)	Mortar target thickness (mm)	Projectile velocity (ms^{-1})	Remarks
101	2.7	9.3	89	Spall
102	2.7	9.3	290	Spall
103	2.7	9.3	408	Spall
104	2.8	18	415	No Spall
105	2.8	18	54	No Spall
106	12.45	22.50	167	6.00/7.50[a]
107	12.50	23.26	391	6.14/7.64[a]
108	12.45	22.52	482	6.02/7.52[a]
109	12.50	22.50	411	0/6.00/7.50[b]
110	12.50	22.50	111	0/6.00/7.50[b]

[a]Distances of transverse/longitudinal PVDF gauges from the impact face (mm).
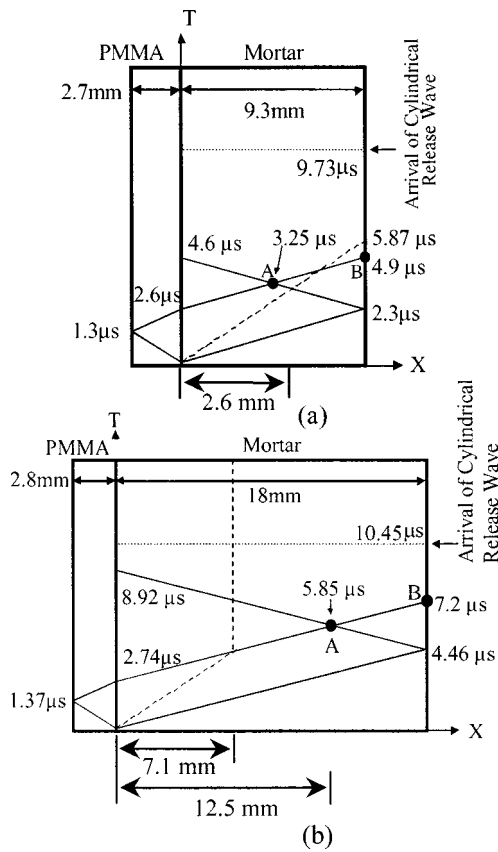[b]Distances of longitudinal PVDF gauges from the impact face (mm).

FIG. 3. Time–distance diagrams for plate impact experiments: (a) when the spall plane is behind the assumed failure wave and (b) when the spall plane is ahead of the assumed failure wave.

FIG. 5. VISAR measurements of free surface velocities: (a) when the spall plane is behind the assumed failure wave and (b) when the spall plane is ahead of the assumed failure wave.

The third set of experiments is designed to investigate the attenuation of the longitudinal stress waves as they propagate through the specimen during impact. To this end, PVDF gauges are positioned at three different locations from the impact face as indicated in Fig. 4(b). The first gauge is placed directly at the impact face, the second one is placed 6

mm into the mortar specimen, and the third one is placed 1.5 mm farther into the interior of the specimen. All the gauges measure longitudinal stress histories at their respective locations. By analyzing the stress histories at different locations, a better understanding can be obtained of how the stress wave attenuates while it passes through the material undergoing damage and failure.

IV. EXPERIMENTAL RESULTS AND DISCUSSION

A. Spall strength of impacted specimens

Figure 5(a) shows the free surface velocity profiles obtained from a set of experiments in which the spall plane lies behind the postulated failure wave as in Fig. 3(a). The three experiments are conducted with impact velocity $V_0 = 89$, 290, and 408 ms^{-1}, respectively. The two lower profiles (for $V_0 = 89$ and 290 ms^{-1}) show distinct drops in the free surface velocity after the initial peak, followed by pull-back increases. The top profile exhibits a slight decrease of velocity after the initial peak. The decreases in velocity are $\Delta V = 10$ ms^{-1}, 8 ms^{-1}, and 3 ms^{-1}, respectively, for the three experiments. Since the velocity drop is related to the spall strength through[20]

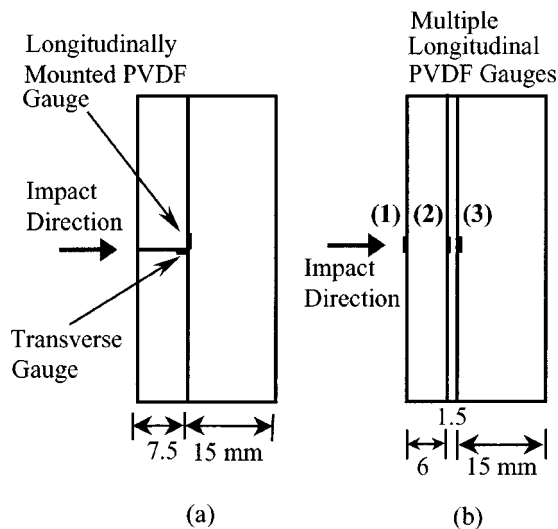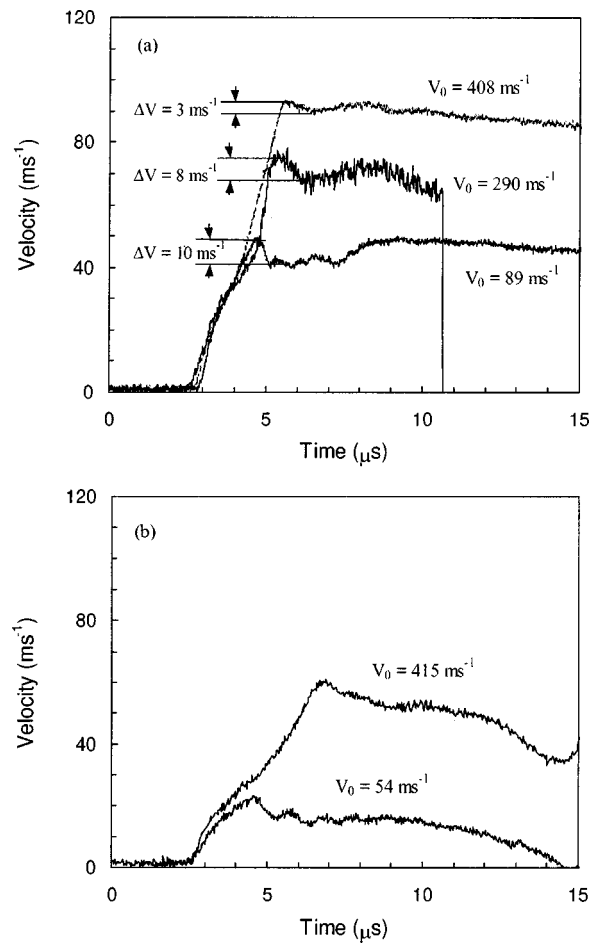$$\sigma_t = \tfrac{1}{2}\rho c \Delta V, \tag{1}$$

FIG. 4. Location of PVDF gauges embedded in the mortar targets: (a) a longitudinal and a transverse gauge for shear strength investigation and (b) three longitudinal gauges for stress wave attenuation investigation.

where these values correspond to spall strengths of 42.3 MPa, 33.9 MPa, and 12.7 MPa, respectively. In the above expression, σ_t, ρ, c, and ΔV denote, respectively, the spall strength, mass density, longitudinal wave speed, and pull-back velocity of the mortar specimen. Clearly, there is a strong dependence of spall strength on impact velocity, indicating the occurrence of damage caused by the initial compressive wave. The observations made here are somewhat similar to those made from spall experiments on glasses.[4] However, the lack of total loss of strength seen here for mortar is in sharp contrast to what has been reported for glasses. In experiments on glasses, full tensile strength is observed if the impact velocity is below a certain critical level and complete loss of strength occurs once this critical impact velocity is reached. Since there is no total loss of spall strength and the spall strength decreases with increasing impact velocity, the damage and failure appear to be a gradual process distinctly different from the sudden and complete loss of tensile strength associated with failure waves in glasses.

The spall strength of 42.3 MPa at $V_0 = 89\,\mathrm{ms}^{-1}$ is very close to or slightly lower than the initial *compressive* strength of the material (45–47 MPa).[21] This indicates that the material possesses its initial tensile strength at this impact velocity. Consequently, it appears that no damage or failure occurs under the conditions of this experiment. At a higher impact velocity of $V_0 = 290\,\mathrm{ms}^{-1}$, the spall strength is 33.9 MPa, indicating the initiation of damage. It appears that a threshold impact velocity between 89 and 290 ms^{-1} is needed to initiate damage in the material. The corresponding input longitudinal and transverse stresses required can be found through

$$\sigma_\mathrm{L} = \frac{(\rho c)_\mathrm{mortar}}{(\rho c)_\mathrm{mortar} + (\rho c)_\mathrm{PMMA}} V_0,$$

$$\sigma_\mathrm{T} = \frac{\nu}{1-\nu}\sigma_\mathrm{L}, \tag{2}$$

where $(\rho c)_\mathrm{mortar}$ and $(\rho c)_\mathrm{PMMA}$ are the longitudinal wave impedances for mortar and PMMA respectively. For $V_0 = 89\,\mathrm{ms}^{-1}$, $\sigma_\mathrm{L} = 69.13\,\mathrm{MPa}$; and for $V_0 = 290\,\mathrm{ms}^{-1}$, $\sigma_\mathrm{L} = 225.25\,\mathrm{MPa}$. These set the upper and lower limits for the threshold input stress required for initiation of damage. The top profile with $V_0 = 408\,\mathrm{ms}^{-1}$ does not show a significant drop in surface velocity before the pull-back increase. Specifically, the drop is only $\Delta V = 3\,\mathrm{ms}^{-1}$, corresponding to a tensile strength of 12.7 MPa. This is an indication of more significant damage in the material.

The curves in Fig. 5(a) show a slow rise of the velocity over time. When the target material is perfectly linear elastic, the rise of the velocity should be instantaneous. Grote *et al.*[21] reported an almost instantaneous rear surface velocity rise for plate impact experiments involving a mortar flyer and a steel target. The initial rising portion of the curve shown in Fig. 5(a) indicates that the material analyzed has a nonlinear stress–strain relation even at low impact velocities. At high impact velocities, the gradual compaction and damage in the material also contribute to the nonlinearity. Similar observations have been reported in experiments on concrete[16] and

glasses.[4,22] However, in the experiments on glasses, much shorter rising times are involved compared with those in experiments on mortar or concrete.

Figure 5(b) shows the velocity profiles obtained from two experiments in which the spall plane lies ahead of the postulated failure wave front, as illustrated in Fig. 3(b). One experiment has an impact velocity of 54 ms^{-1} and the other has an impact velocity of 415 ms^{-1}. Both profiles show overall continuous decrease in surface velocity after the peak. The profile for $V_0 = 54\,\mathrm{ms}^{-1}$ shows a spall signal that indicates a tensile strength of the intact material. This is essentially a fully elastic event without compressive damage, similar to the first experiment in Fig. 5(a) with $V_0 = 89\,\mathrm{ms}^{-1}$. At $V_0 = 415\,\mathrm{ms}^{-1}$, however, the input stress intensity is sufficient to cause damage as suggested by the results shown in Fig. 5(a), the free surface velocity decreases monotonically and no pull-back signal is observed. The impact velocities for the two profiles shown in Fig. 5(b) are significantly different, yet both suggest that the material is quite intact and possesses significant tensile strength in the region ahead of the damaged material. These results lead to two conclusions. The first is that a critical input stress level must be exceeded in order to induce compressive damage. The second is that once the critical input stress level is exceeded there are indeed two regions in the specimen. One of the regions is on the side of the impact face and shows lower levels of spall strength due to damage. The other region is on the side of the rear surface and has significant tensile strength. The fact that no spall is observed in the experiment with $V_0 = 415\,\mathrm{ms}^{-1}$ shows that once damage occurs there is significant dissipation in the material and the attenuation of the stress wave may be sufficient to prevent further damage and spall in far regions of the specimen.

The above results are significantly different from those reported for glasses tested using a similar configuration.[6,22] This behavior also points to a failure process different from the failure wave phenomenon that has been observed in glasses. The transition between the damage zone and the intact zone here in mortar may be gradual and continuous rather than abrupt as in glasses. At least two factors may contribute to causing the differing behaviors. First, the more inhomogeneous microstructure of mortar (compared to glass) can limit the speed of microcrack growth, causing damage and, therefore, loss of strength over longer times rather than appearing to be instantaneous. Second, the attenuation and dispersion of stress waves due to nonlinearity in mortar may cause damage to be spatially nonuniform. The degree of damage and loss of strength can decrease along the direction of impact. Sufficient attenuation and dispersion would eventually preclude further propagation of damage, allowing far regions of the specimen to retain the original spall strength even under high impact velocities that are sufficient to cause damage in regions close to the impact face. The experiments conducted to characterize the attenuation and dispersion of the stress pulse (to be discussed later) provide support for this observation and the interpretation of the results here.
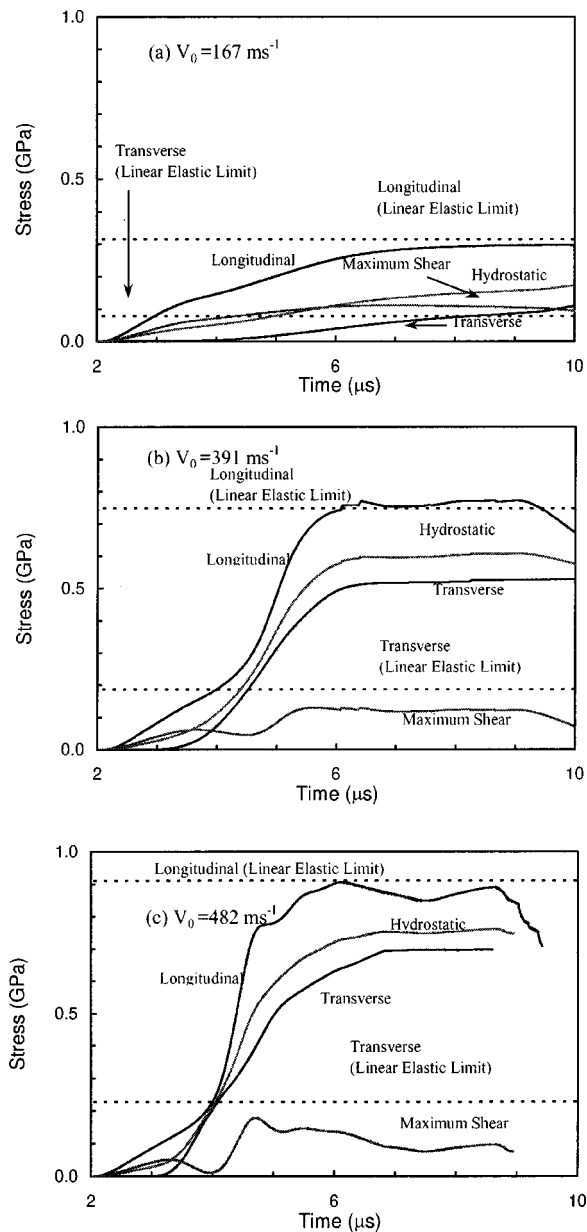
FIG. 6. Longitudinal and transverse stresses measured using PVDF gauges: (a) $V_0 = 167\,ms^{-1}$, (b) $V_0 = 391\,ms^{-1}$, (c) $V_0 = 482\,ms^{-1}$.

B. Shear strength of impacted specimens

In order to gain a better understanding of how damage occurs within mortar during impact loading, a set of experiments are conducted in which internal stress histories are directly monitored by PVDF gauges, as illustrated in Fig. 4(a). The histories of the longitudinal and transverse stresses measured at impact velocities ranging from 167 to 482 ms^{-1} are shown in Figs. 6(a)–6(c). The transverse gauge is located slightly closer to the impact face (1.5 mm) than the longitudinal gauge due to the finite gauge size and the physical constraint associated with gauge insertion. For clear comparison, the longitudinal and transverse profiles are synchronized in this paper, accounting for the distance between the two gauges. Each gauge package has a finite thickness, creating a gap of approximately 100–125 μm between the two sides of the plane of gauge insertion in the specimen. The

closure of this gap takes approximately 0.25–0.75 μs under the impact conditions analyzed. Such times are small compared with the signal rise times observed, indicating the effect of gauge insertion on the overall response is minor and negligible. The measurements indicate that the rise in the longitudinal stress precedes the rise in the transverse stress. The delayed rise of the transverse stress can be attributed to the closure of the gap under the compressive loading. Note that the loading stress pulse ends at approximately $t = 10\,\mu$s. The histories of the maximum shear stress

$$\tau_{max} = \frac{\sigma_L - \sigma_T}{2}, \tag{3}$$

and the hydrostatic pressure achieved in the material

$$p = \frac{\sigma_L + \sigma_T + \sigma_T}{3}, \tag{4}$$

are also shown. The horizontal dash lines in Fig. 6 indicate the stress levels for σ_L and σ_T predicted by one-dimensional linear elastic stress wave theory according to Eq. (2).

The longitudinal and transverse stress histories shown in Fig. 6(a) correspond to the lowest impact velocity considered, or $V_0 = 167\,ms^{-1}$. These profiles show that while the longitudinal stress approaches its linear elastic limit, the transverse stress increases monotonically and slightly exceeds its linear elastic limit toward the end of the loading period. The shear stress increases initially and then saturates at around 110 MPa. Since the longitudinal and transverse stress levels approach their linear elastic limits, there does not appear to be significant failure in the material. The saturation of τ_{max}, however, indicates that slight nonlinearity exists in the material response at this loading level. This nonlinearity may occur elastically without damage or may be due to the onset of damage.

At a much higher impact velocity, the results are quite different. Figure 6(b) shows the stress histories for $V_0 = 391\,ms^{-1}$. While the longitudinal stress approaches and saturates at the elastic limit, the transverse stress exceeds and reaches a level that is more than twice its elastic limit. The maximum shear stress τ_{max} increases until approximately $t = 5.5\,\mu$s. At that moment, it reaches a level of approximately 120 MPa. Note that this level is very close to the shear stress level (110 MPa) maintained by the material in Fig. 6(a). Clearly, although both the longitudinal and transverse stresses are much higher under the higher impact velocity here, the shear stress carried by the material does not increase accordingly. This result points to the occurrence of failure in this higher velocity experiment. Also, it is reasonable to estimate that the shear strength of the material is approximately or slightly lower than 110 MPa. Evidence supporting this estimate is twofold. First, this is approximately the level of shear stress carried by the material at two input stress levels. The inability of the material to carry a higher shear stress at the higher input stress level suggests failure. Second, at the lower input stress level of Fig. 6(a), both the longitudinal and transverse stresses are close to their respective elastically predicted limits, suggesting the condition of that experiment is close to or does not significantly exceed the critical point of failure initiation.
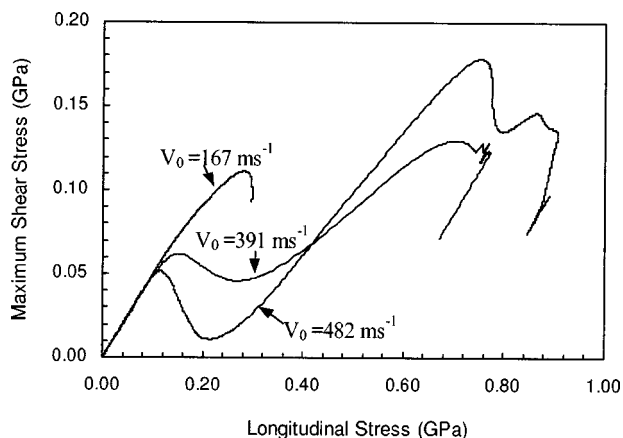
FIG. 7. Shear strength as a function of longitudinal stress.

At an even higher impact velocity of $V_0 = 482 \, \text{ms}^{-1}$ [see Fig. 6(c)], the stress histories show characteristics similar to those in Fig. 6(b). The maximum shear stress τ_{max} reaches a plateau of approximately 130 MPa, slightly higher than that in Fig. 5(b), and subsequently decreases slightly. The average level is around 125 MPa, consistent with those seen in Figs. 5(a)–5(b). Note that failure has clearly occurred in this experiment. The successively higher shear stress levels in these experiments may have to do with the effect of hydrostatic stress on the flow strength of the fragmented and rubblized material. This slight increase in shear strength can be ascribed to the increased hydrostatic pressure in the highest velocity experiment. Hydrostatic pressure enhances internal friction in the rubblized material and the higher internal friction allows higher shear stresses to be carried by the material.[23] According to Eq. (4), the maximum hydrostatic pressures in the three experiments in Fig. 5(a) and 5(b) are, respectively, $p_{max} = 160$, 593, and 767 MPa.

Figure 7 shows the maximum shear stress τ_{max} as a function of longitudinal stress σ_L for each of the three impact velocities considered. The curves are obtained by cross plotting the maximum shear stress and longitudinal stress curves shown in Figs. 6(a)–6(c). These curves show an initial linear region with no damage. The maximum and minimum shear stresses attained decrease with increasing impact velocity. This seems to correlate with the amount of damage in the material. At late stages of loading, the shear stress increases with the longitudinal stress, reflecting the increase of shear resistance due to increase in internal friction in the fully pulverized material.

The transverse stress profiles shown in Fig. 6 are in contrast to those observed for glasses by others.[1,6] A gradual increase in transverse stress is observed here for mortar, indicating the failure process is a rather gradual process of damage development and accumulation. A sharp increase in transverse stress upon arrival of the failure wave is reported for glasses, suggesting a more precipitous drop in shear strength and a more rapid process of failure. On the other hand, the saturation of shear-stress-carrying capability associated with damage and failure observed here for mortar is similar to what is reported for glasses by Brar et al.[1] and Espinosa et al.[6] Both processes limit the shear-stress-

carrying capacity of the materials, regardless of the rate at which failure occurs. Espinosa et al.[7] and Chen and Xin[8] simulated the phenomenon of transverse stress increase during the failure wave propagation using numerical models. Numerical simulations of the more gradual damage and failure process in mortar have not been conducted. The mechanisms are different for the glasses and mortar. In glasses, the initiation and growth of microcracks dominate the failure process. In mortar, material heterogeneities and voids contribute significantly to the deformation.

C. Attenuation of stress waves in impacted specimens

Nonlinearity in material response, damage, and failure cause dispersion and dissipation during the propagation of stress waves. Changes in the loading wave profile as deformation progresses influence subsequent deformation and failure. In Fig. 5, it was found that while spallation occurs in regions of specimens closer to the impact face (within approximately 3 mm) no spallation was observed in regions far away (more than 12.5 mm) from the impact face even at the high impact velocity levels analyzed. Furthermore, a dependence of spall strength on input stress level (impact velocity) is found in regions showing spallation. Since spallation does not occur in regions far away from the impact face even at the high input stress levels analyzed, there should be a strong dissipation and attenuation of the loading wave as it traverses the specimen, especially through damaged regions. To verify this conjecture and to quantify the attenuation, additional experiments are conducted to measure the stress histories at different distances from the impact face. The configuration used is shown in Fig. 4(b). The three longitudinal gauges are located at 0, 6, and 7.6 mm from the impact face, respectively.

The histories of longitudinal stress recorded at the three locations for $V_0 = 111 \, \text{ms}^{-1}$ and 411 ms^{-1} are shown in Figs. 8(a) and 8(b), respectively. At the low velocity of $V_0 = 111 \, \text{ms}^{-1}$, the amplitudes of all three stress profiles are quite consistent. Based on the result in Fig. 6(a), the input stress level (86.2 MPa) is not sufficient to cause damage in the specimen. As expected, the rise time in the stress profile for the impact face is shorter. The general trend shows dispersion of the wave profile. Clearly, no significant stress attenuation occurs over the distances analyzed. At the higher impact velocity of $V_0 = 411 \, \text{ms}^{-1}$, more dispersion is seen in the profiles. The rise times for gauges 2 and 3 (3 μs and 3.5 μs, respectively) are significantly and progressively longer than that for the impact face gauge. Note that this impact velocity corresponds to an input stress level of 319.2 MPa, well above the level needed to cause damage and failure. The increase in rise time and decrease in stress amplitude are more pronounced than those for $V_0 = 111 \, \text{ms}^{-1}$. The amplitude of the stress pulse at gauge 3 is approximately 65% of that at the impact face. These results provide additional evidence for failure at high impact velocities and confirm occurrence of attenuation of the stress pulse which is responsible for preventing damage from occurring at locations relatively far away from the impact face. Espinosa et al.[6] conducted similar tests on soda-lime glass using embedded
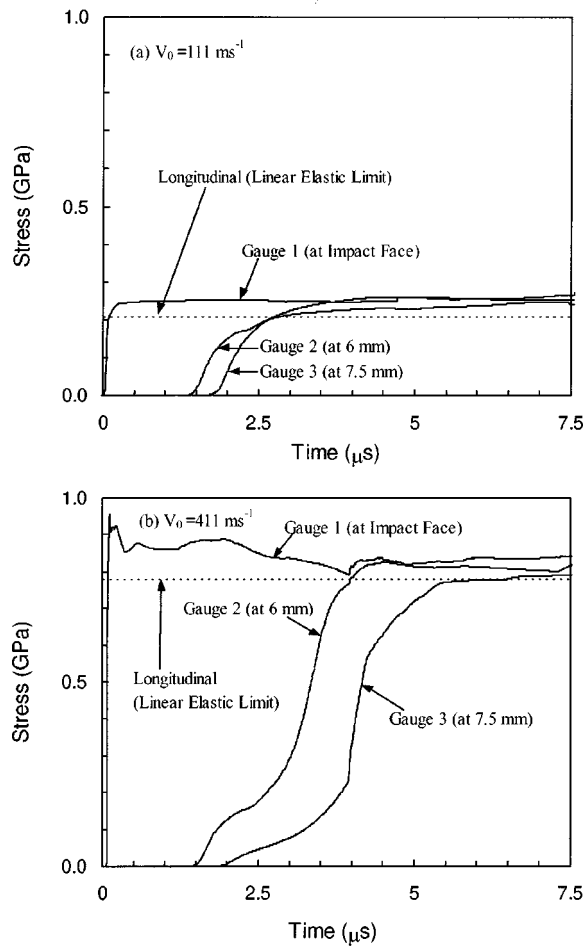
FIG. 8. Longitudinal stresses measured at different locations within the specimen using PVDF gauges: (a) $V_0 = 111 \text{ ms}^{-1}$ and (b) $V_0 = 411 \text{ ms}^{-1}$.

manganin gauges and observed progressively decaying longitudinal stress in the material behind failure wave fronts. The data obtained here are consistent with what has been reported in the literature.

V. CONCLUSIONS

This study has yielded experimental data on the dynamic failure behavior of mortar under the uniaxial strain conditions of normal plate impact. The analysis of spall strength showed evidence of damage behind the compressive loading wave and the absence of damage ahead of the wavefront. This lack of damage is seen even at high impact velocities which are sufficient to generate failure in regions near the impact face. In regions close to the impact face, the spall strength is found to decrease with increasing impact velocity, indicating that a gradual increase in damage occurs with increasing input stress and that the material does not lose all its strength instantaneously. An analysis of the maximum shear stress history confirms that the failure in mortar is indeed a rather gradual process, in contrast to the well-defined failure front and complete loss of tensile strength associated with the failure wave phenomenon that has been reported for glasses. The experiments suggest that the threshold impact velocity needed to initiate damage in mortar is approximately 167 ms^{-1} which corresponds to an input compressive

stress level of 130 MPa. The threshold shear strength under the impact loading conditions considered is approximately 50–110 MPa and appears to be loading rate dependent. While damage accumulates during loading and increases with impact velocity, the comminuted material also exhibits slightly higher shear stress levels at higher hydrostatic pressures. The experimental data obtained do not support the theory of failure waves for mortar. The gradual damage and failure process occur without a clearly defined failure front. The experiments also show that the failure process causes attenuation of the stress wave at high impact velocities and this attenuation is responsible for preventing damage at locations farther away from the impact face.

APPENDIX

Calibration of PVDF gauge for transverse stress measurement

PVDF gauges have long been used to measure the longitudinal stresses in impact experiments. In this study, an experiment is conducted to calibrate their output for measuring the transverse stress under the uniaxial strain conditions of a normal plate impact. The configuration used is illustrated in Fig. 4(a). Both the flyer and the target are made of Hampden tool steel hardened to a hardness of 65 on the Rockwell C scale. The experiment is designed in such a way that both the flyer and the target remain nominally elastic during the impact so that the longitudinal and transverse stresses can be accurately calculated using the elastic stress wave theory. The plates are 76.2 mm in diameter. The flyer has a thickness of 11.79 mm and the target has a thickness of 15.87 mm. The gauge package is approximately 125 μm in thickness. Two leads run along the package and cross where a piezoelectric PVDF film is located. A current viewing resister is soldered to the lead ends. This resistor has a well-characterized resistance ($\pm 0.0001 \ \Omega$) and allows the gauge output to be recorded. Signals from the PVDF sensors are analyzed and converted to stress histories at the locations where the gauges are embedded.

Accounting for the gap closure due to the gauge thickness, the expected stress histories are

$$
\sigma_L(t) = \begin{cases} 0, & \text{if } 0 \leqslant t \leqslant t_0 \\ \frac{1}{2}\rho c V_0 \left(\dfrac{t - t_0}{t_1} \right), & \text{if } t_0 \leqslant t \leqslant t_1 \\ \frac{1}{2}\rho c V_0, & \text{if } t_1 \leqslant t \end{cases}
$$

$$
\sigma_T(t) = \frac{\nu}{1 - \nu} \sigma_L(t), \tag{A1}
$$

where t_0 is the time of stress wave arrival at the gauge location and $t_1 - t_0 = 0.56 \ \mu$s is the rise time of stress pulse due to gap closure, $\rho c = 47.03 \text{ kg m}^{-2}\text{s}^{-1}$ is the longitudinal wave impedance of Hampden steel, and $\nu = 0.288$.

The experiment has an impact velocity of $V_0 = 225 \text{ ms}^{-1}$. The measured and predicted stress profiles are shown in Fig. 9. Dotted lines represent prediction and solid lines represent the measurements. The maximum longitudinal stress calculated from Eq. (A1) is $\sigma_L = 5.29 \text{ GPa}$ and the
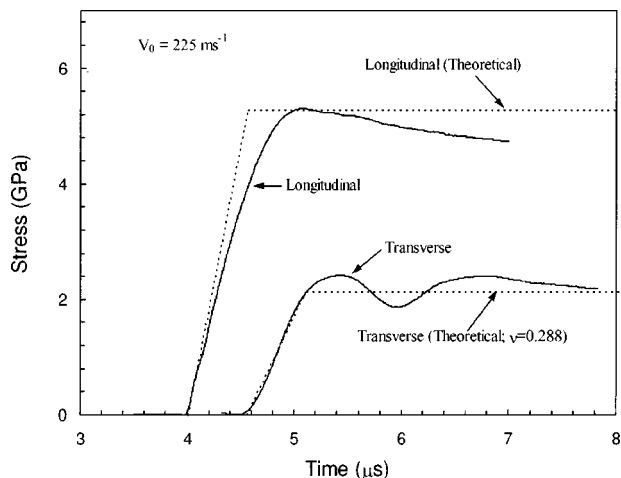
FIG. 9. Longitudinal and transverse stresses in a steel plate; measurements are from PVDF gauges and theoretical predictions are based on the one-dimensional elastic wave propagation.

corresponding transverse stress is $\sigma_T = 2.14$ GPa. The measured maximum longitudinal stress matches the predicted value and the measured maximum transverse stress is 2.4 GPa, yielding an error of 11.6%. A comparison of lateral stresses measured from PVDF and other accepted gauges (such as piezoresistive manganin stress gauges) would be helpful in establishing the validity of PVDF measurements.

ACKNOWLEDGMENT

[1] N. S. Brar, S. J. Bless, and Z. Rosenberg, Appl. Phys. Lett. **59**, 3396 (1991).
[2] G. I. Kanel, S. V. Rasorenov, and V. E. Fortov, *Shock Compression of Condensed Matter*, edited by S. C. Schmidt, R. D. Dick, J. W. Forbes, and D. G. Tasker (Elsevier, New York, 1991), pp. 451–454.
[3] R. J. Clifton, Appl. Mech. Rev. **46**, 540 (1993).
[4] G. F. Raiser, J. L. Wise, R. J. Clifton, D. E. Grady, and D. E. Cox, J. Appl. Phys. **75**, 3862 (1994).
[5] Z. Rosenberg, N. K. Bourne, and J. C. F. Millett, J. Appl. Phys. **79**, 3971 (1996).
[6] H. D. Espinosa, Y. Xu, and N. S. Brar, J. Am. Ceram. Soc. **80**, 2061 (1997).
[7] H. D. Espinosa, Y. Xu, and N. S. Brar, J. Am. Ceram. Soc. **80**, 2074 (1997).
[8] Z. Chen, X. Xin, Int. J. Solids Struct. **36**, 3977 (1999).
[9] J. C. F. Millett, N. K. Bourne, and Z. Rosenberg, *Shock Compression of Condensed Matter-1999*, edited by M. D. Furnish, L. C. Chhabildas, and R. S. Hixon, (AIP, N.Y., 1999), pp. 607–610.
[10] N. S. Brar, and S. J. Bless, High Press. Res. **10**, 773 (1992).
[11] Z. Rosenberg, D. Yaziv, and S. J. Bless, J. Appl. Phys. **58**, 3249 (1985).
[12] G. F. Raiser, Ph.D. thesis, Brown University, 1993.
[13] F. E. Heuze, Int. J. Rock Mech. Min. Sci. Geomech. Abstr. **27**, 1 (1990).
[14] H. He, and T. J. Ahrens, Int. J. Rock Mech. Min. Sci. Geomech. Abstr. **31**, 525 (1994).
[15] T. Sekine, T. S. Duffy, A. M. Rubin, W. W. Anderson, and T. J. Ahrens, Geophys. J. Int. **120**, 247 (1995).
[16] M. E. Kipp, L. C. Chhabildas, and W. D. Reinhart, *Proceedings of the APS Topical Conference on Shock Compression of Condensed Matter*, Amherst, MA, 27 July–1 August, 1997, pp. 557–560.
[17] R. A. Graham, M. U. Anderson, F. Bauer, and R. E. Setchell in *Shock Compression of Condensed Matter-1991*, edited by S. C. Schmidt, R. D. Dick, J. W. Forbes, and D. G. Tasker (Elsevier, 1992), pp. 883–886.
[18] S. P. Sheffield, R. L. Gustavsen, R. R. Alcon, R. A. Graham, and M. U. Anderson, in *High-Pressure Science and Technology*, edited by S. C. Schmidt, J. W. Shaner, G. A. Samara, and M. Ross, (AIP, New York, 1993), pp. 1377–1380.
[19] M. U. Anderson and R. A. Graham, AIP Conf. Proc. **370**, 1101–04 (1996).
[20] L. C. Chhabildas., L. M. Barker, J. R. Asay, and T. G. Trucano, *Proceedings of the APS Topical Conference on Shock Compression of Condensed Matter* Albuquerque, NM, 14–17 August, 1989, pp. 429–432.
[21] D. L. Grote, S. W. Park, and M. Zhou, Int. J. Impact Eng. (submitted).
[22] G. F. Raiser, and R. J. Clifton, *High-Pressure Science and Technology* (AIP, New York, 1994), pp. 1039–1042.
[23] S. W. Park, Q. Xia, and M. Zhou, Int. J. Impact Eng. (submitted).